Journal of Petroleum Science and Engineering 212 (2022) 110198

Contents lists available at ScienceDirect

Journal of Petroleum Science and Engineering

journal homepage: www.elsevier.com/locate/petrol

A fluid dynamic model for Single Well Chemical Tracer tests with variable petrophysical and pre-flushing parameters

T. Pedersen

Institute for Energy Technology, Kjeller, Norway

ARTICLE INFO

Keywords:
SWCT test
Porosity
Permeability
Variable sor
Pre-flushing

ABSTRACT

Porosity and permeability are two fundamental reservoir parameters. We study how important large variations in their values are for residual oil saturation estimates from Single Well Chemical Tracer tests. Although porosity and permeability do not enter the classical chromatography formulae, or variations thereof, that does not necessarily imply that they are irrelevant in all real scenarios. This is because porosity and permeability govern how fluids are distributed within the oil-bearing formation, and thus influence dispersion, temperature, rate of hydrolysis of the primary tracer, pH, partitioning etc., all of which may affect the residual oil saturation estimates. We focus on coarsening and fining upwards sedimentary sequences, but we also consider constant porosity scenarios. In addition, we examine how spatial variations in residual oil saturation influence the single value 'average' obtained by the tracer test. The impact of pre-flushing on the estimated residual oil saturation estimate is investigated as well. An axially symmetric finite element model was developed that calculates fluid flow in the wellbore as well as in the oil-bearing target formation; reservoir cooling caused by the injection of cold brine; transport of solutes in the brine; and pH driven changes in the rate of hydrolysis of ethyl acetate. A Reynolds Averaged Navier-Stokes equation with an algebraic turbulence model was applied in the wellbore to calculate fluid flow there, whereas the Brinkman equation was used in the porous target formation. The temperature of the brine pumped into the target as a function of time was calculated analytically for a down casing model. pH changes induced by the acetic acid produced by the hydrolysis of ethyl acetate are buffered by solutes in the injected brine as well as by calcite in the oil-bearing formation were accounted for. The transport of solutes calculations account for fluid advection, diffusion, dispersion as well as temperature dependent partitioning of ethyl acetate between the residual oil and the injected brine. We use test data based on published values and a brine composition that is realistic for a sandstone reservoir. The synthetic tracer production curves generated by the model vary only modestly between the various porosity, permeability, residual oil saturation and pre-flushing models. A simple and widely used chromatography formula was applied to estimate the residual oil saturation from the synthetic tracer curves. This yields 18–19% for all porosity-permeability scenarios when the true constant value is 22%. We also studied six cases with variable S_{or}. In these cases, the chromatographic formula underestimates the average residual oil saturation by 1–3% except in two models where residual oil saturation increases with increasing porosity; then, the estimate is 8% too low. More work is needed to understand why. In summary, we find that variable porosity and permeability do not significantly increase the estimation error relative to constant models, except when the residual oil saturation varies spatially – then, the error may be much larger. Finally, four pre-flushing models all yield 18% residual oil saturation for a true constant value of 22%, i.e., the error is like the tests without pre-flushing.

1. Introduction

Single Well Chemical Tracer (SWCT) tests are performed to obtain an estimate of the residual oil saturation (S_{or}) in watered out reservoirs (Deans, 1971; Tomich et al., 1973; Deans and Majoros, 1980; Deans and Carlisle, 2007). Such estimates are important for reserve assessment, recovery calculations and to gauge the performance of Enhanced Oil Recovery (EOR) methods like hydrocarbon miscible gas floods (Cockin et al., 2000), low salinity water floods (Skrettingland et al., 2011; Khaledialidusti et al., 2015; Al-Shalabi et al., 2017; Kazemi et al., 2019), and alkaline-surfactant-polymer (ASP) floods (Carlisle et al., 2014; Fortenberry et al., 2016) among others.

E-mail address: tom082012@gmail.com.

https://doi.org/10.1016/j.petrol.2022.110198
Received 25 September 2021; Received in revised form 5 January 2022; Accepted 20 January 2022
Available online 29 January 2022

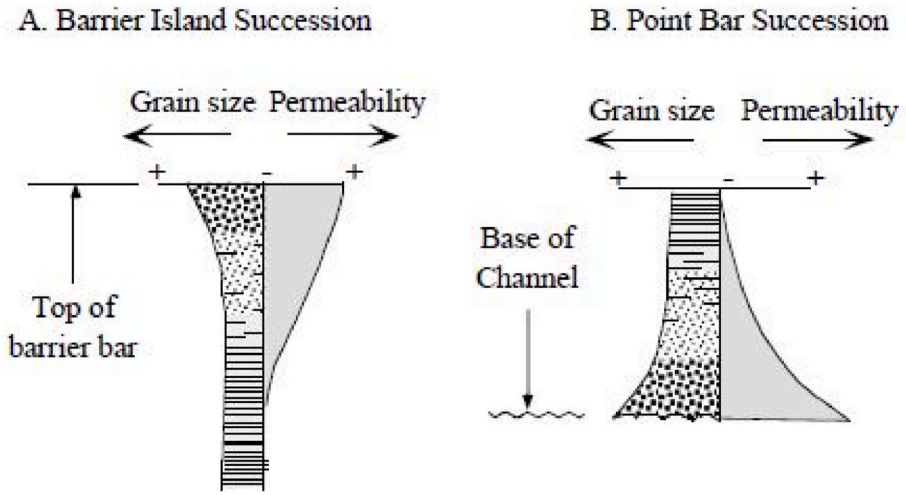

Fig. 1. Generalized porosity and permeability relationships for coarsening (A) and fining upwards (B) sedimentary successions. After Hiatt (2000).

A SWCT test typically starts by pushing brine containing a reactive oil-water partitioning tracer like ethyl acetate (primary tracer) into the oil-bearing formation (e.g., Deans and Majoros, 1980). When the primary tracer is at a distance of a few meters from the wellbore, it is left there for some days to partly hydrolyze into a secondary (quasi) ideal water tracer (ethanol in the case of ethyl acetate). When back production commences, the water tracer travels faster than the partitioning oil-water tracer and their chromatographic separation can be monitored at the wellbore as a function of time or produced volume. S_{or} can then be estimated from the observed separation and the laboratory measured distribution constant (partitioning coefficient) of the oil-water tracer. Deans and Majoros (1980) present an extensive review of the SWCT method while Deans and Carlisle (2007) give an updated discussion. Khaledialidusti et al. (2014) discuss several unconventional (non-chemical) single well models. To the best of our knowledge, none of these have been tested in the field.

A SWCT test yields an average S_{or} estimate for a several cubic meter large rock volume, takes typically 2–3 weeks to complete and may yield 'fair to excellent estimates of S_{or}' in both sandstone and carbonate reservoirs with large variations in temperature, fluid salinity and rock properties (Chang et al., 1988). We estimate that about a thousand SWCT tests have been performed worldwide and this number increases rapidly. Hereafter, we only discuss ethyl acetate as the primary tracer with ethanol as the secondary tracer since this is the case in most SWCT tests performed so far. The success of the SWCT method is thus also evidence of the qualities of ethyl acetate as primary tracer under many circumstances. Producers are the best choice for performing a SWCT test since after extensive water injection, the oil in the pore space surrounding an injection well may no longer be representative for the oil in the reservoir (Deans and Majoros, 1980; Gadgil, 1979).

Ethyl acetate is retarded relative to moving water because it partitions between the water and the stagnant oil, whereas the temperature front between the cold injected brine and the hot reservoir is delayed because the brine gains heat from the hot formation rock it passes through. In addition, the temperature gradient starts to develop once the test begins, whereas ethyl acetate first must travel down to the oil-bearing formation. Fortuitously, the distribution constant of ethyl acetate and the thermal properties of typical target formations are such that in many cases the temperature gradient between the relatively cold injected brine and the hot reservoir fluid, at least to some extent, crosses the ethyl acetate tracer bank (Park, 1989; Park et al., 1991; Pedersen, 2018, 2020, 2021). Since the rate of hydrolysis of ethyl acetate increases exponentially with temperature (International Critical Tables, 1930), such a gradient will produce a horizontal displacement between the primary and secondary tracers when back production commences, often referred to as a 'handicap' (Park, 1989; Park et al., 1991; Pedersen, 2018, 2021, 2021). Acetic acid is a by-product of the hydrolysis of ethyl acetate and will reduce pH, and normally also the rate of ethyl acetate hydrolysis. The acid formed during transit (i.e., injection and production) will move with the water and thus move away from the ethyl acetate so that it will not have much impact on the rate of hydrolysis. During shut-in, however, the acid will not move relative to the ethyl acetate and both pH and the rate of hydrolysis in the primary tracer bank may be lowered significantly. This effect might also impact the S_{or} estimate (Wellington and Richardson, 1994a, 1994b, 1994c; Ghosh, 1994; Deans and Ghosh, 1994; Khaledialidusti and Kleppe, 2018; Pedersen, 2020, 2021). However, there is yet no consensus on how important this effect is (Khaledialidusti et al., 2014; Pedersen, 2021).

In this study, we incorporate temperature gradients as well as pH driven rate of hydrolysis changes in the SWCT models. We also calculate the unavoidable dispersion that occurs in any real SWCT test. It has been suggested (Deans and Majoros, 1980; Shook et al., 2009) that dispersion can be included simply by using the mean residence times of the primary and secondary tracers in the chromatographic formula of Cook (1971) to estimate S_{or}. Pedersen (2020, 2021) demonstrated, however, that this in some cases may increase the S_{or} estimation errors because in a real scenario also other factors than dispersion come into play and these are not considered by the mean residence time model.

Most SWCT tests assume that porosity and permeability are constant within the oil-bearing rock where the test is performed. In some studies, however, the oil-bearing formation is divided into several layers, each of with have different petrophysical parameters. A recent example is the work of Kazemi et al. (2019) from Greater Burgan – the world's largest sandstone reservoir. Carbonate reservoirs formations often contain local heterogeneities that prevent some of the pore space from being accessible to the flowing fluid. In such regions, transport of tracers is governed by diffusion. 'Dead-end' (e.g., Coats and Smith, 1964) and 'pore-diffusion' models (Deans and Carlisle, 1986) have been developed to analyze SWCT test results in such two compartment (flowing and stagnant fractions) rocks.

In this contribution, we investigate another type of reservoir heterogeneity – coarsening and fining upwards sedimentary sequences. As the name implies, they are characterized by large and systematic variations in grain size, and thus porosity and permeability. This will influence how the injected brine is distributed within the formation and thus potentially the S_{or} estimate. In addition, we also investigate constant porosity scenarios with porosity and permeability values from 10 to 30%, and 1 to 1000 mD, respectively.

Coarsening upwards facies successions are typical of prograding shoreface and deltaic environments and exhibit increasing grain size and

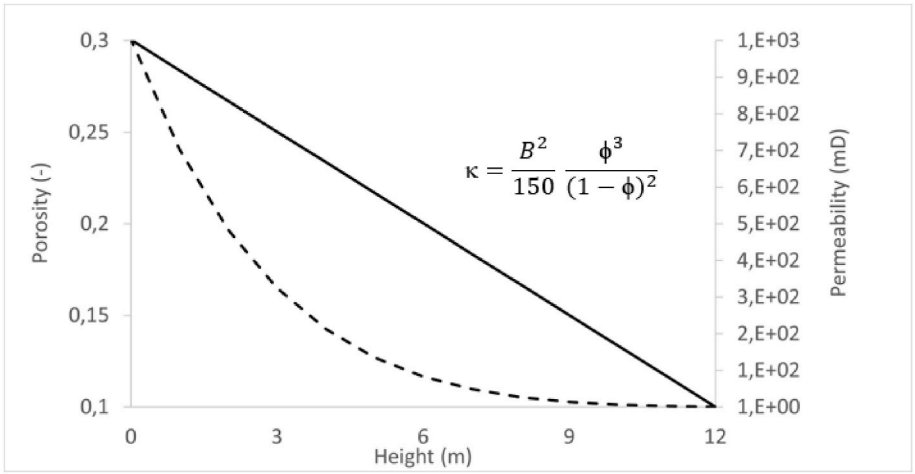

Fig. 2. Porosity (solid) and permeability (dashed) for the fining upwards sequence as a function of height above the base of the 12 m thick target formation. The porosity-permeability model is based on data in Ramon and Cross (1997) and the Kozeny-Carman equation (embedded) where κ is permeability, φ is porosity and B is a fitting parameter (the product of grain size and grain sphericity, but that does not matter for our purpose). The number 150 considers tortuosity. See main text for further explanation. The impermeable (zero permeability) shales above and below the target formation have a porosity equal to zero (all symbols, values, units, and definitions are presented in Table 1).

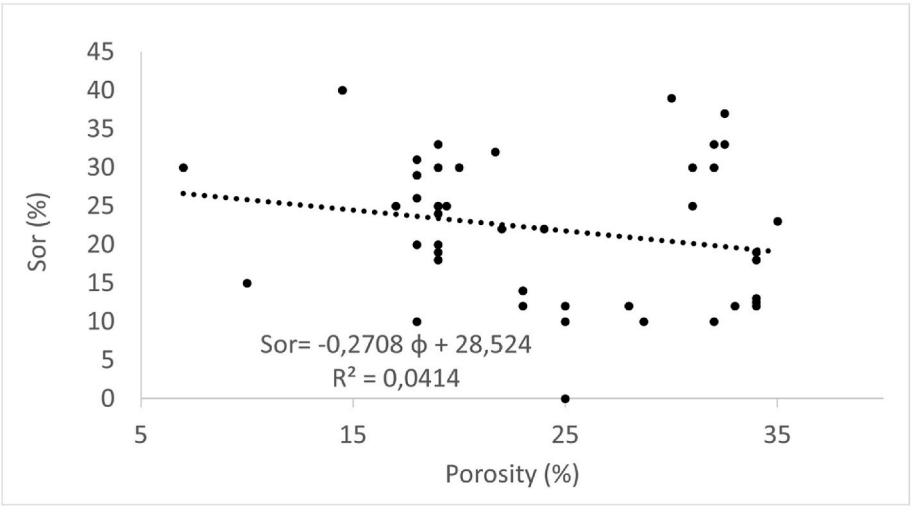

Fig. 3. Porosity versus Sor for 48 SWCT tests (Deans and Majoros, 1980). Also shown is a linear trendline and a relation between φ and S_{or} as well as the correlation factor R squared. This only confirms what can be seen visually; that there is no significant correlation between porosity and S_{or}.

permeability within each succession (Hiatt, 2000) (Fig. 1A). In contrast, fining upwards sedimentary facies successions are characteristic of fluvial environments, such as point bar deposits (i.e., the convex banks of meander bends) (Hiatt, 2000). They show a decrease in grain size and permeability moving up the succession (Fig. 1B).

Usually, the velocity of the injected brine in the oil-bearing target is input to SWCT test models. Assuming that the brine is incompressible, and that the velocity does not depend on depth, one finds that the velocity decreases as the reciprocal distance from the wellbore. In our case, however, the fluid velocity distribution (vertically and horizontally) is unknown and must be solved for as a function of injection rate, wellbore configuration and flow conditions (laminar or turbulent), as well as the geometry, porosity, and permeability of the oil-bearing formation. We believe that ours is the first dynamic (rather than kinematic) SWCT model that realistically considers both the fluid flow in the wellbore and in the porous target formation.

The quantitative porosity-permeability model is based on data published by Ramon and Cross (1997). We estimate that for a fining upwards formation the porosity may decrease from 30 to 10% as a function of height above the base of the target formation, whereas the permeability decreases from 1000 mD to 1 mD. We use the Kozeny-Carman equation (Fig. 2) to calculate the permeability as a function of porosity within the target formation and arrive at the porosity-permeability distribution depicted in that figure. For the coarsening upwards sequence, the reverse relationships are assumed to be true. We have made no effort to define typical or average porosity and permeability functions for coarsening and fining upwards sequences. However, for a generic study like this contribution, we think that the porosity-permeability model illustrated in Fig. 2 should be sufficient to examine the importance of porosity and permeability variations. In a real SWCT test, reservoir specific porosity and permeability parameters should be applied. The curves in Fig. 2 are for 100% water saturation, i.e., S_{or} equal to zero. For a non-zero S_{or} value, the porosity and thus permeability are reduced since then the porosity in the Kozeny-Carman equation is replaced by the effective porosity (see below).

Fig. 3 depicts porosity versus S_{or} for the 48 SWCT tests published by Deans and Majoros (1980) that gave a S_{or} estimate. Considering the relatively large number of SWCT tests from different locations, it seems unlikely that there should exist a universal relationship between porosity and S_{or}.

Although a SWCT test only yields a single S_{or} value, that does not mean that it is not interesting to investigate what influence variations in S_{or} have on that estimate – after all, a strictly uniform S_{or} value within the oil-bearing formation is not realistic. Specifically, we want to examine the effect of variable S_{or} in our four porosity models. Fig. 3 shows *average* values for each formation, and it does not necessarily

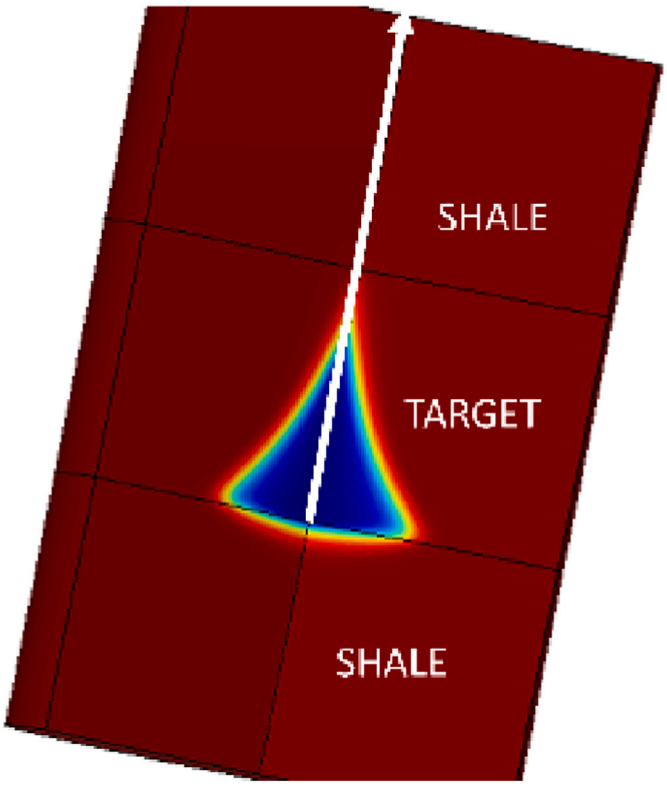

Fig. 4. The axially symmetric SWCT model configuration used in this paper (i.e., the model appears unchanged if rotated around the wellbore). The permeable target formation ('Target') is found between impermeable shales (denoted 'Shale'). The white arrow represents the wellbore. Assuming an axially symmetric model makes it possible to obtain a realistic 3D solution by solving the differential equations for fluid flow, temperature, and solute transport in the 2D plane labeled 'Target' and 'Shale' (above and below the target) on the right side only. This is computationally a very efficient approach relative to a full 3D model with the same parameters since it mathematically reduces a 3D problem to a 2D problem. The wellbore is tilted for illustrational purposes only and is closed at the bottom of the target formation. The figure shows the temperature distribution at the end of the injection phase for the fining upwards case. The thickness of the target formation, H*, is 12 m and the same is its width, W. The impermeable shales above and below the target formation have the same dimensions. The depth to the target formation, d_0, is 3000 m. The colors refer to the temperature at the end of the injection phase. Blue is cold and red is hot. (For interpretation of the references to color in this figure legend, the reader is referred to the Web version of this article.)

follow that there is no correlation between porosity and S_{or} *within* the individual formations. Unfortunately, very little work has been published on this matter as far as we know. One way to address this problem would be to derive porosity-S_{or} relationships from theoretical reasoning. It seems difficult, though, to obtain reliable quantitative correlations by such an effort. Instead, we decided to combine several highly different S_{or} distributions with the four porosity models – this should in our view be sufficient to evaluate whether variable Sor has a significant impact on the S_{or}* estimates. The variable S_{or} distributions are discussed in detail in the Model section.

A prerequisite for the SWCT method to work is that the oil in the target formation is at residual oil saturation. A 98% or higher water-cut is often considered a practical criterion for the oil to be virtually immobile (Deans and Majoros, 1980). If the well has a significant oil-cut, pre-flushing with brine may be performed before the SWCT test proper to reduce the remaining oil saturation to residual (e.g., Carlisle et al., 2014). We note that the SWCT itself includes pre-flushing because: 1. When the injection of the primary tracer commences, brine will immediately start to flood the oil-bearing formation, whereas the tracer first

Table 1
Symbols, values [units], and descriptions.

Symbol	Value Unit	Description
A	0.021 [K/m]	Geothermal gradient
A	Eq. (18) [m]	Temperature parameter
B	10 [°C]	Earth's surface temperature
B	Eq. in Fig. 2. [m^2]	Kozeny-Carman fitting parameter
C_F	0.55 [-]	Forchheimer parameter
C_i	Eq. (33) [mol/m^3]	Concentration of solute number i
C_I	Table 2 [mol/m^3]	Injection concentration
Cp	4180 [J/K/kg]	Specific heat water
$C_{V,eff}$	Eq. (19) [J/m^3/K]	Effective volumetric heat capacity
$C_{V,or}$	1.67 10^6 [J/m^3/K]	Residual oil volumetric heat capacity
$C_{V,r}$	2.41 10^6 [J/m^3/K]	Rock volumetric heat capacity
$C_{V,w}$	4.18 10^6 [J/m^3/K]	Water volumetric heat capacity
d	Eq. (17) [m]	Depth
D_{Dl}	Eq. (37) [m^2/s]	Longitudinal dispersion
D_{Dz}	Eq. (38) [m^2/s]	Transverse dispersion
D_F	10^{-9} [m^2/s]	Diffusivity
d_o	3000 [m]	Depth to target formation
F	Eq. (1) [N]	Body forces
F	Eq. (18) [-]	Time function (Ramey, 1962)
G	Eq. (5) [1/m]	Reciprocal wall distance
H	[m]	Height above base of target
H*	12 [m]	Target formation and shale thicknesses
I	Eq. (1) [-]	Identity matrix
J	Eq. (39) [mol/(m^2s)]	Flux of solute number i
K	Eq. (1) [Pa]	Viscous stress tensor
K	Eq. (36) [1/s]	Ethyl acetate hydrolysis rate
K	Eq. (35) [-]	Distribution constant
k_a	Eq. (36)	Acid catalysis factor
K_{eq}	Eq. (33) [Variable]	Equilibrium constant
$k_{P,i}$	Eq. (33) [m^3/kg]	Adsorption isotherm for solute number i
$\mathbf{K_r}$	Eq. (9) [Pa]	Rock stress tensor
k_s	Eq. (36)	Base catalysis factor
K_w	Fig. (6) [mol^2/m^6]	Water dissociation constant
l^+	Eq. (3) [-]	Normalized distance from wall
l_{ref}	Eq. (6) [m]	Wall reference distance
l_w	Eq. (3) [m]	Distance from wall
N	Eq. (13) [-]	Normal vector
P	Eq. (1) [N/m^2]	Pressure
Q	Eq. (22) [W/m^2]	Heat flux
Qinj	450 bbl/d	Injection rate
Qprod	480 bbl/d	Production rate
R	Fig. 3 [m]	Radial distance from center of wellbore
r_0	0.09 [m]	Well radius
$R_{e,w}$	Eq. (3) [-]	Wall Reynold's number
R_i	Eq. (33) [mol/m^3/s]	Reaction term solute i
S_{or}	10-30 [%]	Residual oil saturation
S_{or}*	Eq. (43) [fraction]	Average Sor estimate from tracer curves
S_{or}'	Eq. (44) [fraction]	Average Sor estimate from Sor distribution
S_s	20 000 [ppm]	Salinity
S_w	Eq. (20) [%]	Water saturation
T	K or °C	Temperature
T	Eq. (1) [s]	Time
T_0	10 [°C]	Brine surface temperature
T_I	Fig. 5 [°C]	Fluid injection temperature
Tinj	1 [d]	Injection period
tprod	6 [d]	Production period
tpush	1 [d]	Push period
T_R	73 [°C]	Initial reservoir temperature
tshut-in	6 [d]	Shut-in period
T_{us}	Eq. (24) [K or °C]	Upstream
U	Variable [m/s]	Fluid velocity
U	Eq. (13) [m/s]	Inlet velocity
u^+	Eq. (7) [-]	Normalized velocity
u_τ	Eq. (7) [m/s]	Shear (friction) velocity
W	12 [m]	Model width
W*	0.83 [kg/s]	Mass injection rate
Z	Fig. 2 [m]	Height
α_l	10^{-3} [m]	Longitudinal dispersivity
α_z	0.5α_r [m]	Transvers dispersivity
B	Eq. (11) [1/m]	Forchheimer coefficient
ΔH	Eq. (24) [J]	Enthalpy change
K	Eq. (9) [md]	Rock permeability
λ_e	2.5 [W/m/K]	Thermal conductivity Earth
λ_{eff}	Eq. (21) [W/m/K]	Effective thermal conductivity

(*continued on next page*)

Table 1 (*continued*)

Symbol	Value Unit	Description
λ_{or}	0.12 [W/m/K]	Residual oil thermal conductivity
$\lambda_{sandstone}$	3.00 W/m/K	Sandstone matrix thermal conductivity
λ_{shale}	2.45 W/m/K	Shale matrix thermal conductivity
λ_w	0.6 [W/m/K]	Water thermal conductivity
M	0.001 [Pa s]	Fluid molecular viscosity
μ_T	Eq. (7) [Pa s]	Turbulent or eddy viscosity
ρ_b	2650 [kg/m^3]	Dry bulk density
ρ_b	1000 [kg/m^3]	Fluid density
σ_W	0.2[-]	Constant in Eq. 5
T	Eq. (33) [-]	Tortuosity
τ_w	Eq. (4) [Pa]	Shear stress at wellbore wall
Φ	Fig. 2 [-]	Target formation porosity
φ_{eff}	$\varphi(1 - S_{or})$ [%]	Effective porosity of target formation
φ_{sh}	0 [%]	Shale porosity
Ω	Eq. (44) [m^3]	S_{or} volume

must travel down the wellbore to the target. 2. The primary tracer will move slower than the brine because of the partitioning between oil and brine, and thus lags behind the waterfront. Using a multicomponent, two-phase SWCT model, Gadgil (1979) demonstrated that pre-flushing can strip the residual oil of light ends and hence reduce S_{or} and change the oil composition, as well as the distribution constant. In this study, we investigate the impact of pre-flushing on the estimated S_{or} by pumping brine into the target formation before the SWCT test proper, but without considering multicomponent or two-phase effects, i.e., we assume that the formation already is at residual oil saturation. Future work should combine two-phase, multicomponent flow with the temperature and pH modeling in this study. Notwithstanding, since the primary tracer due to partitioning moves well behind the waterfront that displaces the oil (ignoring fingering), our results should, at least as a first-order approximation, be valid also when the oil saturation is above residual.

The main objective of this paper is thus to investigate how variations in porosity, permeability, residual oil distribution, and pre-flushing may influence the residual oil saturation estimate. To this end, we have developed a numerical finite element model using the partial differential equations software package COMSOL Multiphysics (COMSOL Multiphysics, 2020) that is well suited for problems like ours where several types of physics are connected (fluid flow, heat transfer and transport of solutes). We estimate S_{or} (denoted S_{or}*) by the simple and widely applied chromatographic formula of Cook (1971). This formula, and variations of it, are probably the most common methods applied to derive S_{or}* in sandstone reservoirs, and that is our principal rational for employing it in this paper. More advanced modeling are often required, particularly in complex cases, to obtain a good estimate of S_{or}.

1.1. Model

The numerical model includes the wellbore as well as the surrounding sedimentary formations (Fig. 4). It is axially symmetric which is not only very efficient from a computational point of view, but in our opinion also the best choice for a generic study like ours. Implicitly, or explicitly, the assumption of axial symmetry around the wellbore is common. Fault and fractures, rock heterogeneities, diagenetic effects etc. may violate the symmetry assumption. However, we would argue that to understand to what extent porosity and permeability variations influence S_{or} estimates in a general sense, this should be of only secondary importance. We also assume that there is no fluid drift in the reservoir and that the remaining oil is immobile, i.e., at residual saturation.

1.2. Fluid velocity and pressure

For a system where an open wellbore (free fluid) is in contact with a porous rock adjacent to it, we use the Navier-Stokes equation in the open part and the Brinkman equation (an extension of the Darcy equation that considers viscous stresses) in the porous rock (Bars and Worster, 2006). This formulation yields pressure and fluid velocity distributions that are continuous across the interface between the wellbore and the porous rock. There is, however, a stress discontinuity caused by the stress absorbed by the rigid porous matrix (Bars and Worster, 2006). With the parameters in Table 1, the flow in the wellbore is fully turbulent (the Reynolds number is about 6000). We use the RANS (Reynolds-Averaged Navier-Stokes) yPlus turbulence model (COMSOL Multiphysics, 2020) to solve for the velocity and pressure fields. This is an algebraic (zero order) turbulence model based on the distance to the nearest wall and is founded on Prandtl's mixing-length theory. We have that

$$\rho_f \frac{\partial \mathbf{u}}{\partial t} + \rho(\mathbf{u}\nabla)\mathbf{u} = \mathbf{F} - \nabla[-p\mathbf{I} + \mathbf{K}] \tag{1}$$

where ρ_f is fluid density (all symbols are explained in Table 1), **u** is velocity, t is time, **F** denotes body forces, p is pressure, **I** is the identity matrix and **K** is the viscous stress tensor

$$\mathbf{K} = (\mu + \mu_T)\left(\nabla\mathbf{u} + (\nabla\mathbf{u})^T\right) \tag{2}$$

in which μ is the molecular viscosity, and the turbulent, or eddy, viscosity, μ_T, is calculated from Eqs. (3)–(6):

$$\mathrm{Re}_w = \frac{\rho_f |\mathbf{u}| l_w}{\mu} = \frac{|\boldsymbol{u}|}{u_\tau} \bullet \frac{\rho_f u_\tau l_w}{\mu} = u^+ l^+, \; u^+ = g(l^+) \tag{3}$$

in which Re_w is the wall Reynolds number, l_w is distance from the wall, u_τ is the shear, or friction, velocity equal to

$$\sqrt{\tau_w / \rho_f} \tag{4}$$

where τ_w is the shear stress at the wellbore wall. u^+ and l^+ are the normalized velocity and wall distance, respectively. The reciprocal wall distance, G, is found by solving the equation:

$$\nabla G \bullet \nabla G + \sigma_w G(\nabla \bullet \nabla G) = (1 + 2\sigma_w)G^2 \tag{5}$$

G is related to l_w as

$$l_w = \frac{1}{G} - \frac{l_{ref}}{2} \tag{6}$$

where l_{ref} is a reference distance and σ_w in Eq. (5) is a small constant. Finally, the eddy viscosity is calculated from the expression:

$$\mu_T = \mu\left(\left(\frac{df}{dl^+}\right)^{-1} - 1\right) \tag{7}$$

The molecular viscosity is a macroscopic property of the fluid whereas the turbulent viscosity is a function of the fluid flow. The turbulent viscosity may be several orders of magnitude larger than the molecular viscosity. For an incompressible fluid, we in addition have that mass conservation requires that

$$\rho_f \nabla \mathbf{u} = 0 \tag{8}$$

In the porous domain, the Brinkman equation reads

$$\frac{1}{\varphi}\rho_f \frac{\partial \mathbf{u}}{\partial t} + \frac{1}{\varphi}\rho_f(\mathbf{u} \bullet \nabla) \bullet \mathbf{u}\frac{1}{\varphi} = \nabla[-p\mathbf{I} + \mathbf{K}_r] - \left(\frac{\mu}{\kappa} + \beta\rho_f|\mathbf{u}|\right)\mathbf{u} + \mathbf{F} \tag{9}$$

Here, φ is porosity, κ is permeability, and the porous rock stress tensor, K, is:

$$\mathbf{K}_r = \mu\frac{1}{\varphi}\left(\nabla u + (\nabla u)^T\right) - \frac{2}{3}\mu\frac{1}{\varphi}(\nabla \bullet u) \bullet \mathbf{I} \tag{10}$$

$(\beta\rho_f|\mathbf{u}|)\mathbf{u}$ is the viscous force component with the Forchheimer coefficient β defined as:

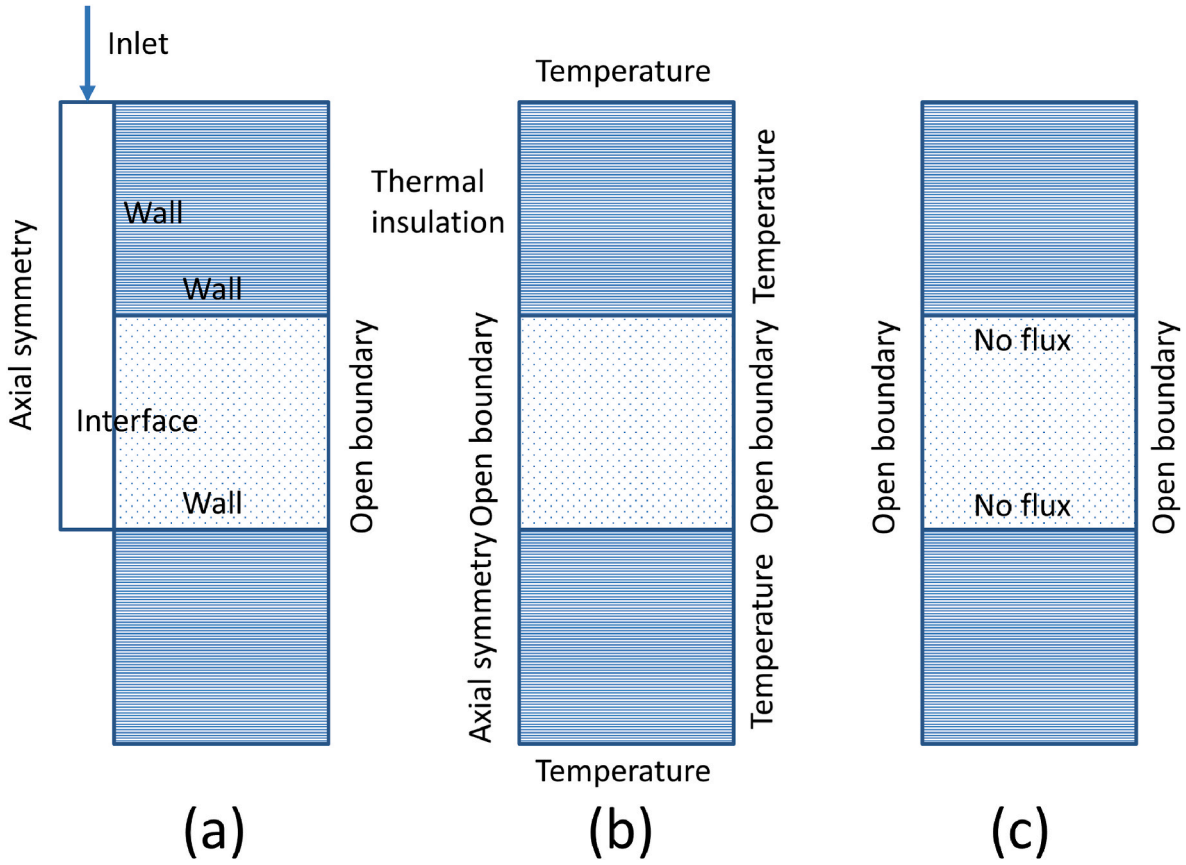

Fig. 5. Boundary conditions for (a): fluid flow, (b): temperature; (c): transport of chemical species. See main text for explanation.

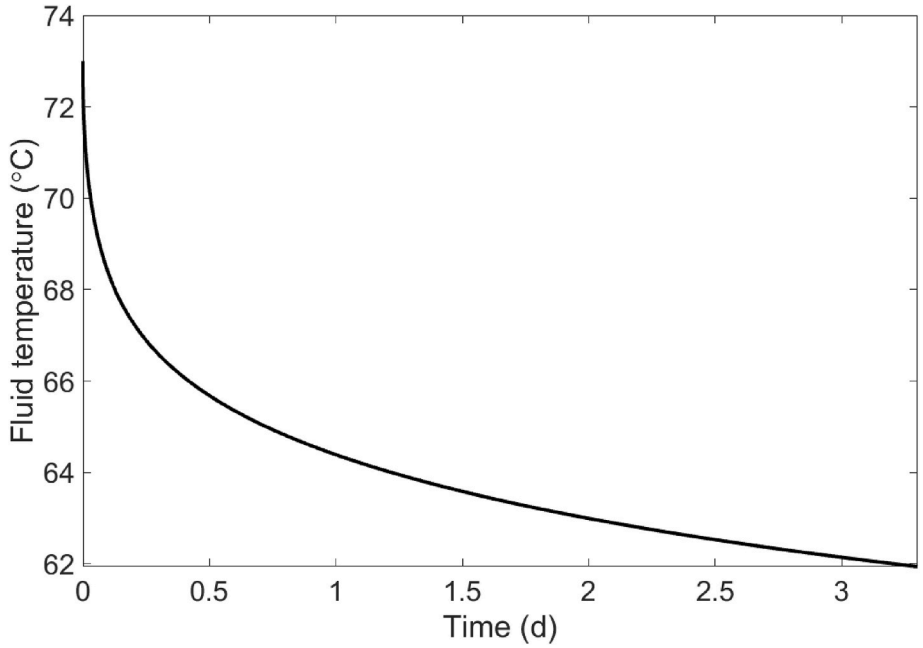

Fig. 6. Injection temperature as function of time derived from Eqs.(17) and (18) with the parameters in Table 1.

$$\beta = \frac{c_F}{\sqrt{\kappa}} \tag{11}$$

where c_F is the Forchheimer parameter. Also in the target formation the fluid is incompressible, i.e.,

$$\rho_f \nabla \mathbf{u} = 0 \tag{12}$$

The boundary conditions for fluid flow in the open wellbore as well as in the porous target formation are defined in Fig. 5a.

Fig. 5a illustrates the boundary conditions for the fluid flow model.

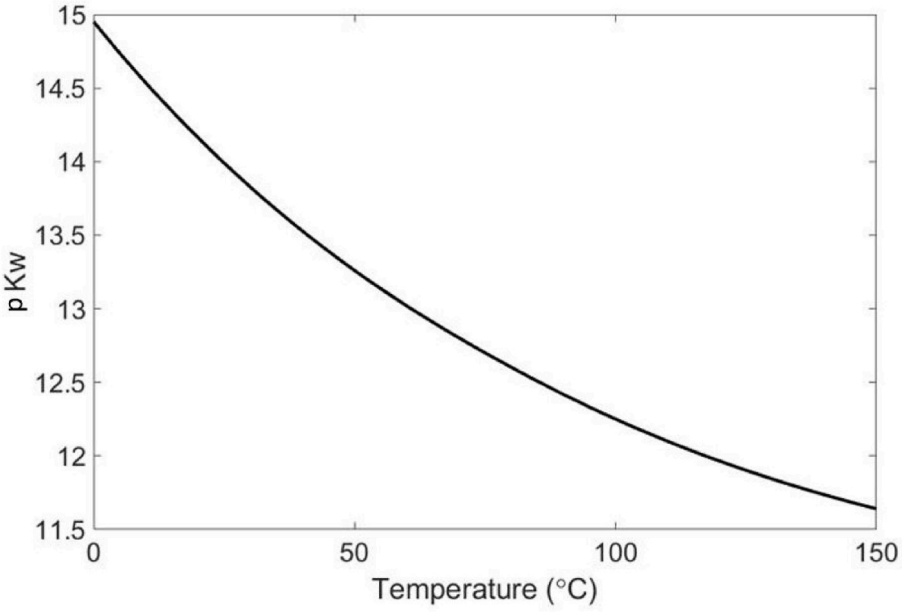

Fig. 7. pKw as a function of temperature. Based on Bandura and Lvov (2006).

The fluid inlet is a normal inflow velocity, **u**, condition with

$$\boldsymbol{u} = -U\bullet\mathbf{n} \tag{13}$$

where

$$U = U(t) = Q(t)/\pi r_0^2 \tag{14}$$

in which Q is the injection or production rate, r_0 is the wellbore radius and **n** is the outwards normal vector at the wellbore inlet (Fig. 5a). The duration of injection, push, shut-in, and back production are given in Table 1. The open boundary condition, i.e., where the fluid leaves or enters the target formation is zero normal stress, i.e.,

$$-[\mathrm{p}\bullet\mathbf{I} + \mathbf{K}_r]\bullet\mathbf{n} = 0 \tag{15}$$

The third boundary condition is the wall (no slip) condition

$$\mathbf{u}(\mathrm{l_w} = 0) = 0 \tag{16}$$

where in the porous target formation $l_w = 0$ and in the wellbore $l_w = h\perp/2$. The initial fluid velocity and pressure are zero everywhere.

1.3. Injection temperature

For a wellbore-rock system initially at thermal equilibrium, Ramey (1962) derived an approximate expression for the brine temperature in the wellbore as a function of depth, d, and time, t:

$$T(d,t) = ad + b - aA + (T_0 + aA - b)exp\left(-\frac{d}{A}\right) \tag{17}$$

in which d is depth, a is the geothermal gradient of the Earth, b is the surface geothermal temperature, and T_0 is the surface temperature of the injected brine. For injection down casing,

$$A = \frac{W^* Cpf(t)}{2\pi\lambda_e} \tag{18}$$

where W* is the injection rate measured in kg s^{-1}, C_p is the specific heat of the injected fluid, λ_e is the thermal conductivity of the Earth and f is a mathematical function. More complex expressions exist for other wellbore configurations. The function f is defined in Ramey (1962) (his Fig. 1 – 'cylindrical source'). Fig. 6 illustrates the brine temperature calculated from Eq. (17) as a function of time with the parameters in Table 1; this temperature is used as the injection temperature TI in the simulations. Parameter values are again given in Table 1 and temperature boundary conditions are illustrated in Fig. 5b.

An eminent feature in Fig. 6 is that there is a smooth decrease in the temperature of the injection fluid with time. If we had used an abrupt temperature change like for example Park (1989) and Park et al. (1991) did, our simulations show that it would have been difficult to avoid using unrealistically high dispersivity values to stabilize the combined temperature and pH dependent hydrolysis rate numerical calculations. More important is, however, that such a smooth temperature change would appear to be more realistic. Pedersen (2018) demonstrates how properly designed fluorescent nanoparticles co-injected with the primary tracer can yield information on the real temperature history during a SWCT test, and thus potentially improve S_{or}*.

1.4. Rock temperature

The temperature, T, in the permeable target formation as well as in the impermeable shales is calculated by solving the heat equation:

$$C_{V,eff}\frac{\partial T}{\partial t} + (C_V)_w\,\overrightarrow{u}\nabla T = \nabla\left(\lambda_{eff}\nabla T\right) \tag{19}$$

in which the effective volumetric heat capacity, $C_{V,eff}$, is:

$$C_{V,eff} = \varphi\left\{C_{V,or}S_{or} + C_{V,w}S_w\right\} + (1-\varphi)C_{V,r} \tag{20}$$

where *or*, *w* and *r* refer to residual oil, water, and rock, and S_{or} and S_w are the residual oil and water saturation, respectively. In a two-phase system, we have that

$$S_w = 1 - S_{or} \tag{21}$$

λ_{eff} is the effective thermal conductivity:

$$\lambda_{eff} = \varphi\{\lambda_{or}S_{or} + \lambda_w S_w\} + (1-\varphi)\lambda_r \tag{22}$$

and λ_{or} and λ_w are the thermal conductivity of residual oil and water, respectively, and λ_r is the rock thermal conductivity of sandstone or shale. The hydrolysis reaction of ethyl acetate is slightly exothermic, but at the tracer concentrations used in SWCT tests, its effect on temperature can be ignored.

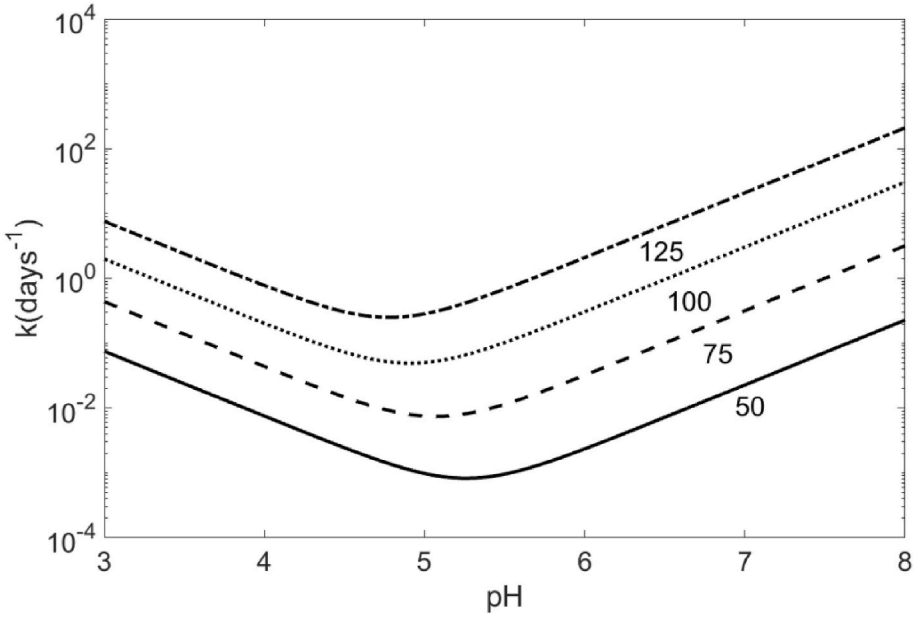

Fig. 8. Ethyl acetate rate of hydrolysis as function of pH and temperature in °C. Based on International Critical Tables (1930) and pKw (Fig. 6). Note logarithmic y axis.

The boundary conditions for the thermal calculations are defined in Fig. 5b. At the boundaries labeled 'temperature', the temperature is equal to the reservoir temperature, TR. At the thermal insulation boundary, we have that $-\mathbf{q}\bullet\mathbf{n} = 0$ where **q** is heat flux. At the two open boundaries, where we must consider that the fluid will flow in different directions during injection and production, we have that

$$\mathbf{u}\bullet\mathbf{n} < 0 : -\mathbf{n}\bullet\mathbf{q} = \rho\Delta\mathrm{H}\mathbf{u}\bullet\mathbf{n} \tag{23}$$

$$\mathbf{u}\bullet\mathbf{n} \geq 0 : -\mathbf{n}\bullet\mathbf{q} = 0 \tag{24}$$

where the change is enthalpy is

$$\Delta H = \int_{T_{us}}^{T} C_P dT \tag{25}$$

T is again temperature and T_{us} is the upstream temperature. The last boundary condition is axial symmetry (Fig. 5b). The initial rock temperature is TR.

1.5. Chemical reactions and solute transport

Ethyl acetate hydrolyzes to produce ethanol and acetic acid according to the reaction:

$$Ethyl\ Acetate + H_2O \rightarrow Ethanol + Acetic\ Acid \tag{26}$$

In addition, our model includes several equilibrium reactions:

$$Acetic\ Acid \leftrightarrow H^+ + Acetate\ Ion^- \tag{27}$$

with the equilibrium constant, K_{eq} (for concentrations in mol l^{-1} (i.e., M) – in the simulations we use the SI unit mol m^{-3}):

$$K_{eq} = 1.8\ 10^{-5} \tag{28}$$

and the dissociation of water equilibrium reaction:

$$H_20 \leftrightarrow H^+ + OH^- \tag{29}$$

The water dissociation constant, K_W,

$$K_W = [H^+][OH^-] \tag{30}$$

depends on temperature (Fig. 7).

The ethyl acetate concentration in the brine when it enters the target formation (C_I) is 40 mol m^{-3} (=0.04 M) (cf. Fig. 5c). The buffering due to carbonate species is modeled by three equilibrium reactions (Ghosh, 1994; Deans and Ghosh, 1994):

$$H_2CO_3 \leftrightarrow H^+ + HCO_3^- \tag{31}$$

$$HCO_3^- \leftrightarrow H^+ + CO_3^{--} \tag{32}$$

$$CaCO_3(s) \leftrightarrow Ca^{++} + CO_3^{--} \tag{33}$$

The equilibrium constants for the first two reactions at reservoir conditions are $10^{-6.4}$ and $10^{-10.3}$, respectively, and the solubility product of calcite (Eq. (33)) is $10^{-8.3}$ (Plummer and Busenberg, 1982).

The transport of the various solutes in the target formation is described by the equation:

$$\left(\varphi_{eff} + \rho_b k_{P,i}\right)\frac{\partial C_i}{\partial t} + \mathbf{u}\nabla C_i = \nabla\left[\left(D_D + \frac{\varphi_{eff}}{\tau}D_F\right)\nabla C_i\right] + \varphi_{eff}R_i \tag{34}$$

Here, φ_{eff} is the effective porosity equal to $\varphi(1 - S_{or})$, ρ_b is the dry bulk density, $k_{P,i}$ is the adsorption isotherm, C_i is concentration, D_D is dispersion, τ is tortuosity, D_F is diffusion, R_i is a reaction term and i refers to solute number i. For ethyl acetate $R = -kC_{Ethyl\ Acetate}$, whereas for ethanol and acetic acid, $R = kC_{Ethyl\ Acetate}$. The adsorption isotherm is

$$k_P, i = \frac{S_{or}\varphi_{eff}\ K}{\rho_b(1 - S_{or})} \tag{35}$$

for ethyl acetate, and zero for the other solutes. K is the distribution constant (partitioning coefficient) and the other terms have been defined earlier. We use the following expression for the ethyl acetate K value as function of temperature and salinity (Deans and Majoros, 1980):

$$K = \left\{2.4 + \left(1.0 + \frac{S_s}{24,000}\right)(0.018T - 5.197)\right\} \tag{36}$$

where we have neglected K's dependency on the tracer concentration because this effect is small (Deans and Majoros, 1980). S_s is salinity measured in ppm while temperature T is measured in Kelvin. The retardation factor, i.e., the velocity of brine divided by the velocity of ethyl acetate, is given by $1 + KS_{or}/(1 - S_{or})$, and is independent of

Table 2
Brine composition and pH used in the model. The model also includes calcite in the target formation. C_I is the concentration of ethyl acetate when injected. The data may represent a sandstone with calcite cement. Modified from Ghosh (1994).

C_I [mol/m^3]	Ca^{++} [mol/m^3]	CO_3^- [mol/m^3]	HCO_3^- [mol/m^3]	H_2CO_3 [mol/m^3]	pH [-]
40	1500	$3.34\ 10^{-6}$	0.0035	$4.62\ 10^{-4}$	7.3

porosity and permeability. It does, however, depend on temperature (Eq. (36)) and varies also with changes in S_{or}.

The overall reaction rate for the hydrolysis of ethyl acetate to ethanol, k, depends on $[H^+]$ and $[OH^-]$ (International Critical Tables, first edition 1930):

$$k = k_a[H^+] + k_b[OH^-] \tag{37}$$

in which k_a and k_b are the acid and base catalysis factors, respectively. Fig. 8 illustrates k (note the logarithmic scale) as a function of pH and temperature. We note that the hydrolysis rate minimum depends on temperature.

We calculate the tortuosity in the target formation from the Millington and Quirk (1961) formula $\tau = \varphi^{-1/3}$. Dispersion parameters are derived from the expressions (Bear, 1979):

$$D_{Dl} = \alpha_l \frac{u_l^2}{|u|} \tag{38}$$

and

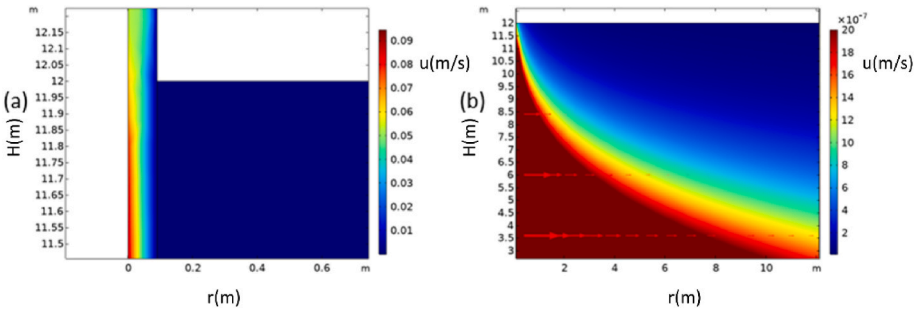

Fig. 9. Fluid velocity during injection in the right half of wellbore (a) and in the porous target formation (b) for the fining upwards sequence with S_{or} decreasing linearly from 33% at the bottom of the target to 11% at the top of it. The r axis represents the distance from the center of the wellbore and the H axis is height above the base of the target formation. In the brown region in (b), the velocity is higher than $2{\cdot}10^{-6}$ m/s. The huge differences in velocity in the two domains is the reason why we choose to use two illustrations. The length of the arrows in (b) is proportional to the logarithm of the fluid velocity. (For interpretation of the references to color in this figure legend, the reader is referred to the Web version of this article.)

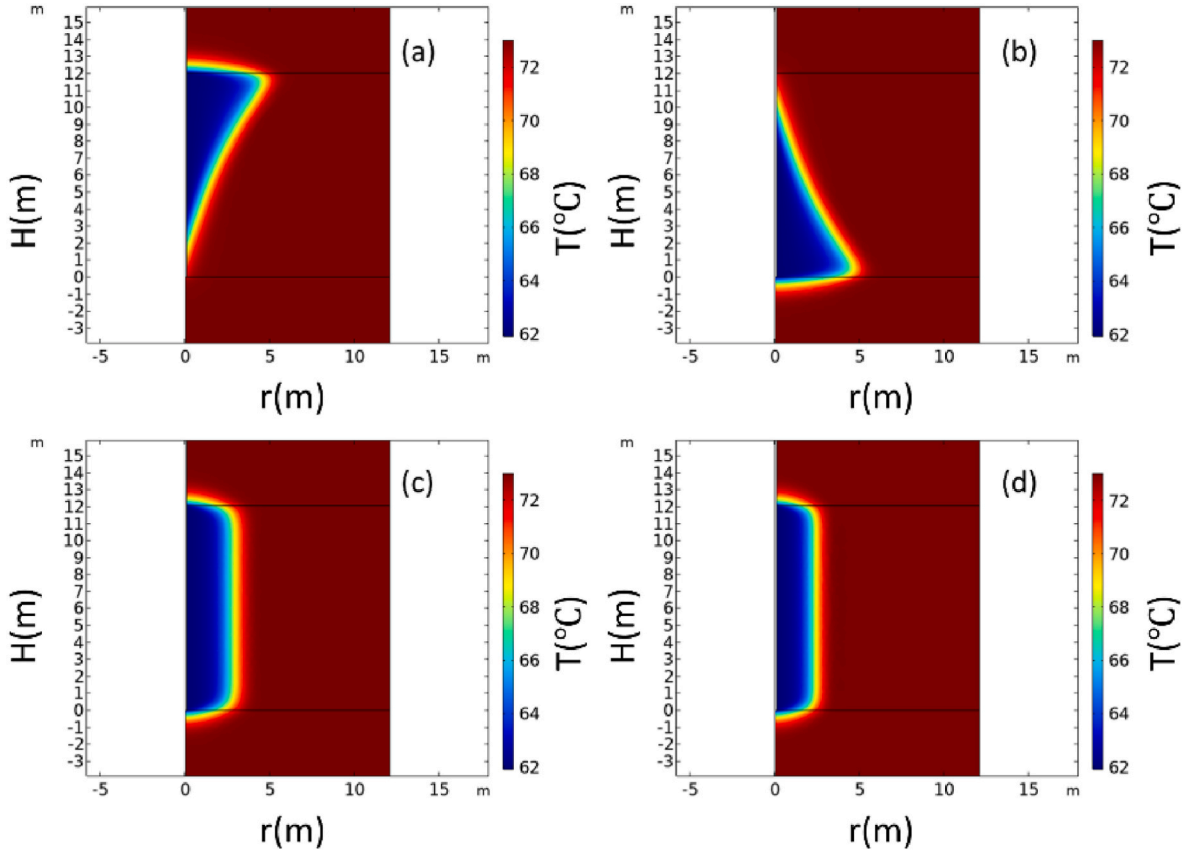

Fig. 10. Temperature in a vertical plane adjacent to the wellbore (at the left, see also Fig. 4) at the beginning of shut-in. r is distance from wellbore center (m) and H is height (m) above the base of the target formation that is located between 0 and 12 m. (a): coarsening upwards. (b) fining upwards. (c): constant porosity (10%) and permeability (1 mD). (d): constant porosity (30%) and permeability (1000 mD). Sor is equal to 22% in all four cases.

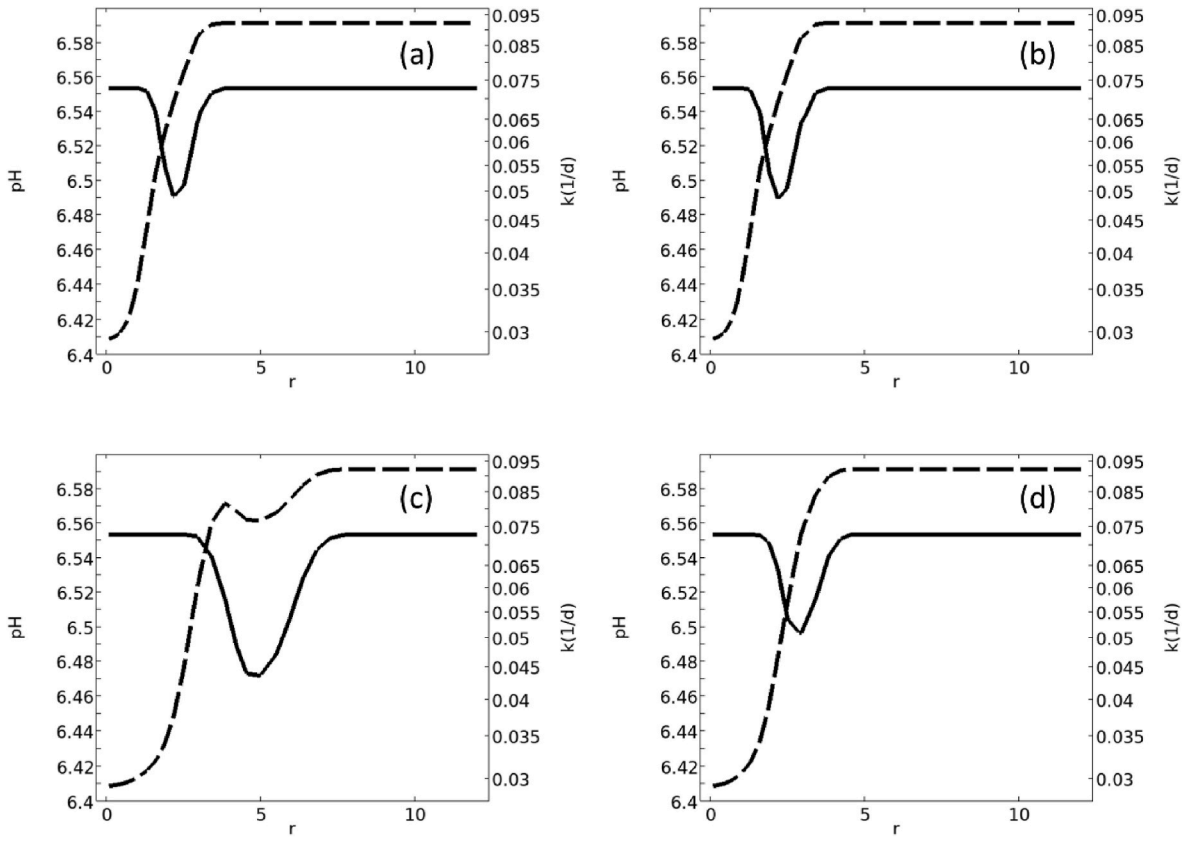

Fig. 11. pH (solid) and k (dashed) as functions of distance from the center of the wellbore at the beginning of shut-in on a horizontal plane located at a height of 6 m (same as Fig. 8). (a): coarsening upwards. (b) fining upwards. (c): constant porosity (10%) and permeability (1 mD). (d): constant porosity (30%) and permeability (1000 mD).

$$D_{D_z} = (\alpha_l - \alpha_z)\frac{u_z^2}{|u|} \tag{39}$$

where α_l and α_z are the longitudinal and transverse dispersivities, respectively.

The boundary conditions for the transport of solutes are illustrated in Fig. 5c. At the No flow boundaries, we have that

$$-\mathbf{n}\bullet\mathbf{J}_i = 0 \tag{40}$$

whereas at the Open boundaries

$$\mathbf{n}\bullet\mathbf{u} > 0 : -\mathbf{n}\mathbf{J}_i = 0 \tag{41}$$

$$\mathbf{n}\bullet\mathbf{u} < 0 : \ C_i = C_{0,i} \tag{42}$$

$\mathbf{J}_i$ is the flux of solute number i.

The set of equations above are solved using the finite element PDE software COMSOL Multiphysics (2020). The mesh consists of triangular elements with higher resolution near the wellbore because that is where most of the variations take place. Time stepping is performed by a second order implicit backward differentiation formula (BDF). It takes typically between 15 min and 1 h to solve a model on a 64-bit computer with two processors and 128 GB RAM memory.

1.6. S_{or} estimates

As discussed in the Introduction, S_{or} is estimated from the synthetic tracer concentration curves by the direct application of Cook's (1971) chromatography formula:

$$E(S_{or}) = S_{or}^{*} = \frac{t_{Ethyl\ Acetate} - t_{Ethanol}}{t_{Ethyl\ Acetate} + t_{Ethanol}(K-1)} \tag{43}$$

in which t is the time when the concentrations of ethyl acetate or ethanol are at their maximum (peak) measured from when back production commences and K is again the distribution constant (Eq. (36)). It is interesting to examine the accuracy of Eq. (43) since it only requires back-of-the-envelope calculations and because it remains widely used either in its original form or with modifications (e.g., Deans and Majoros, 1980; Shook et al., 2009; Doorwar et al., 2020). Obviously, if we had used the same model to analyze the tracer curves that we used to derive them, we should have obtained almost perfect results. One of the advantages of using a model to generate synthetic tracer curves is that we know the exact value of all parameters involved, S_{or} included.

1.7. Variable S_{or}

We define six possible relationships between porosity and S_{or} within the oil-bearing formation: 1: A coarsening upwards sequence with S_{or} going linearly from a low value (11%) at the base of the formation to its maximum (33%) at the top of the formation. The 11 and 33% values lie symmetrically around the average value of 22% (Table 1) and cover the majority of published S_{or} results. 2: A fining upwards formation with the same S_{or} distribution as in model 1. 3: constant 10% porosity with S_{or} equal to 11% from zero to 6 m above the bottom om the oil-bearing formation, and 33% between 6 m and its top. 4: A constant 30% porosity with S_{or} equal to 33% between zero and 6 m, and 11% between 6 m and 12 m above the bottom of the target formation. 5: A model like model 1 except that the S_{or} distribution is reversed. 6: A model like model 2 except that the S_{or} distribution is reversed. In all six models, permeability is given by the relationship in Fig. 2. The results for these six scenarios are discussed after the presentation of the constant S_{or} cases. Note, we do not argue that these S_{or} distributions are found in any specific location, only that they in combination with the highly variable

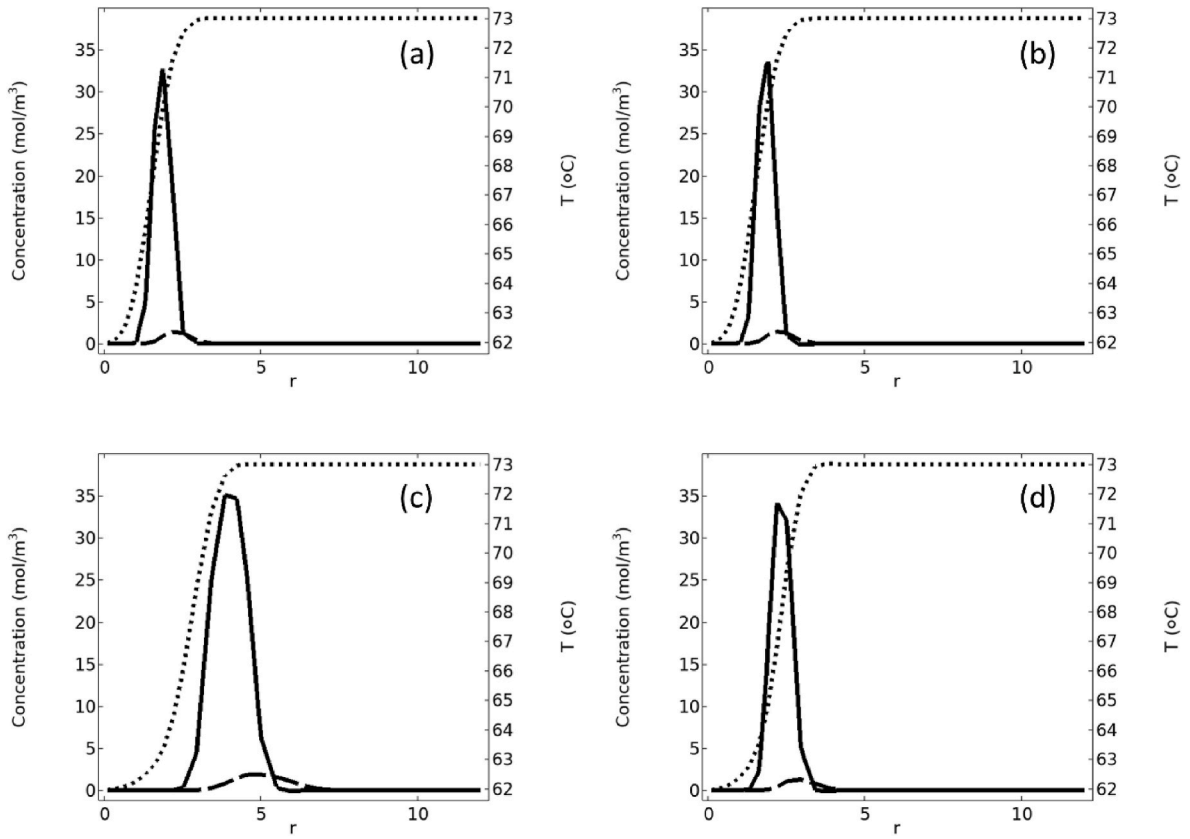

Fig. 12. Concentration of ethyl acetate (solid), ethanol (dashed) and temperature (dotted) at the beginning of shut-in at a horizontal plane located at a height of 6 m, i.e., in the middle of the oil-bearing formation. r is distance from the wellbore center. (a): coarsening upwards. (b) fining upwards. (c): constant porosity (10%) and permeability (1 mD). (d): constant porosity (30%) and permeability (1000 mD).

porosity-permeability models provide an envelope within which most real distributions will be located.

In a variable S_{or} scenario, we also must evaluate what the 'true' average S_{or} is directly from the known S_{or} distribution within the volume, Ω, 'examined' by the SWCT test – we denote this average S_{or}'. Then, we can compare S_{or}' with S_{or}* to evaluate the performance of the SWCT test. If S_{or} is constant, this problem does not arise, of course. We define S_{or}' as:

$$S'_{or} = \frac{\int S_{or} d\Omega}{\int d\Omega} \tag{44}$$

where Ω is the volume of the oil-bearing formation between the wellbore and the surface defined the center of mass of the ethyl acetate concentration when shut-in ends. Since the concentration curve is close to symmetric, this yields essentially the same result as using the maximum concentration would have given. Eq. (44) yields an approximate 'average' S_{or} 'seen' by the SWCT test.

1.8. Pre-flushing

Typically, the pre-injection brine is pumped out to about 3–6 m from the wellbore before the SWCT test proper begins (www.chemtracers.com); in this study, a value of 6 m is used. The injection rate is kept constant (Table 1), so the time required to reach 6 m varies between the porosity-permeability models. For the coarsening and fining upwards models, the average porosity is applied to calculate the pre-flushing brine volume.

1.9. Test data

As in Pedersen (2020, 2021), we define a generic or representative (approximate arithmetic averages) SWCT test and rock data set (Table 1) based on Tables 5–1 in Deans and Majoros (1980). Their table contains data from 59 SWCT tests mostly in sandstones although a few limestone cases are included as well. We only include the ethyl acetate primary tracer tests data. For chemical modeling, we use in addition the chemistry data in Table 2.

2. Results

Fig. 9 shows fluid velocities for a fining upwards sequence. Note that the velocity field cannot be described as a constant over the distance from the wellbore, the almost universally adopted velocity field in the SWCT literature. Since porosity and permeability variations are common in oil bearing formations, this is a potentially important if S_{or} varies with height or distance since then the tracers will sample the oil-bearing formation non-uniformly.

Fig. 10 illustrates the temperature at the beginning of shut-in in a vertical plane from the wellbore and outwards for four different porosity and permeability scenarios. We note how thermal conduction causes cooling of the impermeable shales above and below the target formation when the relatively cold brine injected into the target formation moves outwards from the wellbore. Lower porosity means that the brine moves further into the oil-bearing formation. This is because a larger rock volume is required to accommodate the injected fluid when the porosity decreases. The low temperatures reduce the rate of ethyl acetate hydrolysis as well as the distribution constant (Eq. (36)) that enters the expression for S_{or}* (Eq. (43)). It is difficult to understand that after five decades of SWCT testing, temperature effects are almost universally

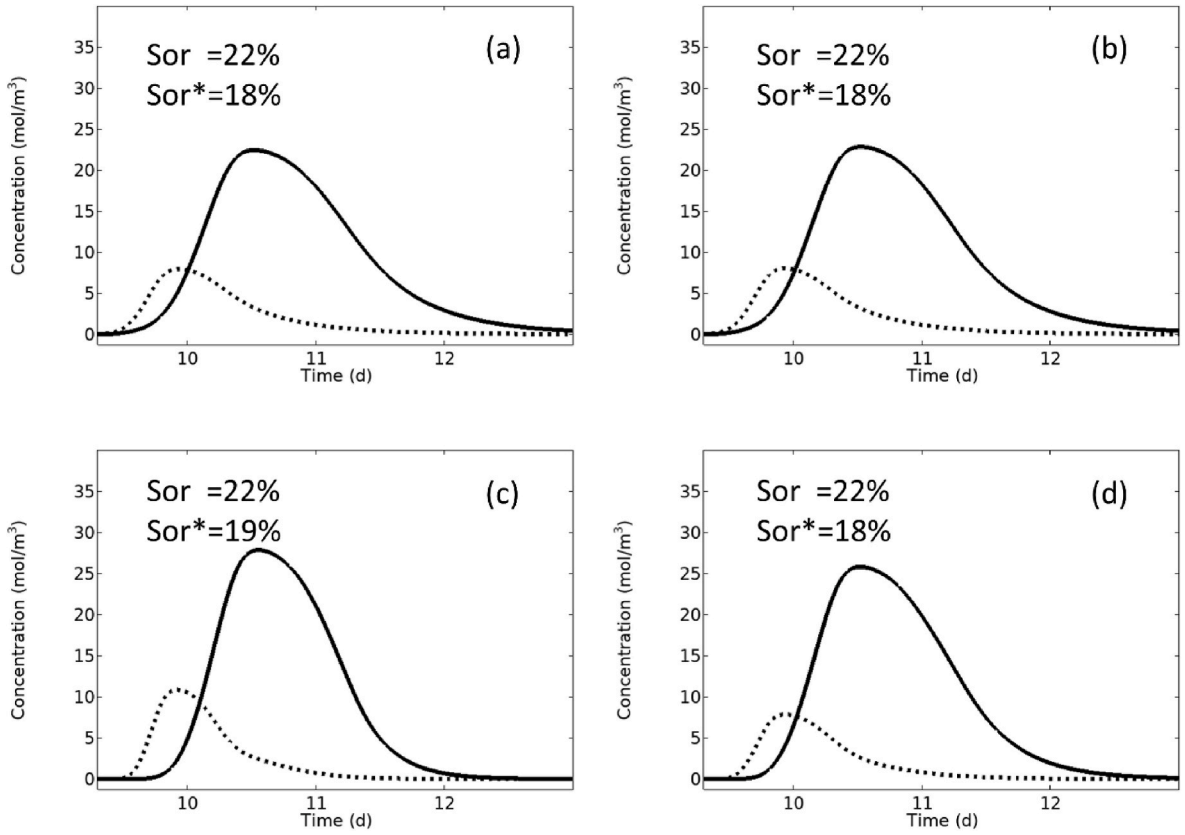

Fig. 13. Synthetic tracer production curves as functions of time starting at the end of shut-in. The solid curve is for ethyl acetate and the dashed is for ethanol. Also included is the S_{or}* value from Eq. (43). (a): coarsening upwards. (b) fining upwards. (c): constant porosity (10%) and permeability (1 mD). (d): constant porosity (30%) and permeability (1000 mD).

ignored, or handled in an oversimplified manner.

pH and the rate constant k when shut-in commences are depicted in Fig. 11. The strong buffer effect of the injected brine solutes and the sandstone diagenetic calcite cement results in only an insignificant reduction in pH due to the acetic acid; about 0.06 units. The reduction in the rate constant due to the fall in pH is thus also small - it is only discernible in Fig. 9 (c) where we have the largest pH reduction. In the other three cases, the increase in the rate of hydrolysis caused by the temperature gradient across the primary tracer overwhelms the reduction due to the small fall in pH. The acetic acid generated is constantly removed from the tracer bank since it moves with the water (cf., Wellington and Richardson, 1994a). Since a real SWCT injection 'pulse' has a finite width, there will normally be an overlap (see also Fig. 10) between the primary tracer bank and the acetic acid, so that the lowered pH nevertheless will cause a reduction in the hydrolysis of the primary tracer. In the rare cases with sandstones devoid of calcite cement, or in the common scenario with oil-wet carbonate reservoirs, or with a brine lean in buffering solutes, the pH reduction caused by the acetic acid may be much larger (Ghosh, 1994; Pedersen, 2020, 2021).

Fig. 12 illustrates the concentrations of ethyl acetate and ethanol as well as temperature when shut-in begins. There is virtually no difference between the coarsening and fining upwards models (Figs. 10 (a) and 8 b)) – but this is hardly surprising since the porosity and permeability are identical at the mid-plane. Only small amounts of ethanol have been generated at this stage; this agrees with the results of Ghosh (1994) and Pedersen (2020, 2021). Because ethanol moves with the water, it is somewhat displaced outwards relative to the ethyl acetate tracer curves. This small amount of ethanol consequently adds to the 'handicap' caused by the temperature gradient across the primary tracer bank previously discussed by Park (1989), Park et al. (1991) and Pedersen (2020, 2021). Because the injected brine volume is the same in all models, the fluid moves much further into the oil-bearing formation when the porosity is 10% instead of 30% (see (Fig. 10 (c) vs. (Fig. 10 (d)). We note that the temperature distribution is less sensitive to this porosity difference than the concentrations of the primary and secondary tracers are. This result was first pointed out by Park (1989). We see that the temperature gradient between the rock's initial temperature (73 °C) and the cold injected brine (minimum approximately 62 °C) is located closer to the wellbore than the primary tracer bank for the 10% porosity case. For the 30% porosity case, however, the temperature gradient crosses the primary tracer bank, and this causes a larger difference in the rate of ethyl acetate hydrolysis across the tracer bank.

The synthetic ethyl acetate and ethanol tracer curves generated by the numerical simulations of models a-d are presented in Fig. 13. Visually, it is difficult to identify any differences between the four models. In other words, the different porosity and permeability models yield only slightly different tracer curves. Because these are the basis for calculating S_{or}*, not only for Eq. (43), but for any method, our results confirm that the SWCT method is robust to variations in not only porosity, but also to highly variable permeabilities that also govern how the injected brine is distributed within the oil-bearing formation. We note that there are hardly any differences between the S_{or}* estimates for the porosity and permeability models a, b, and d, whereas the result for model c is approximately 1% closer to the true S_{or} value of 22%. The main reason is that for a porosity of only 10%, the primary tracer is pushed so far into the target that the temperature curve is relatively flat (Park, 1989; Park et al., 1991; Pedersen, 2020).

We observe from Fig. 13 that Eq. (43) consistently underpredicts S_{or}* with 3–4% relative to the true value of 22%. This is in excellent agreement with the interval 3–5% that Pedersen (2020, 2021) arrived at in studies with constant porosity and permeability, but with large variabilities in brine composition, reservoir petrology and other model

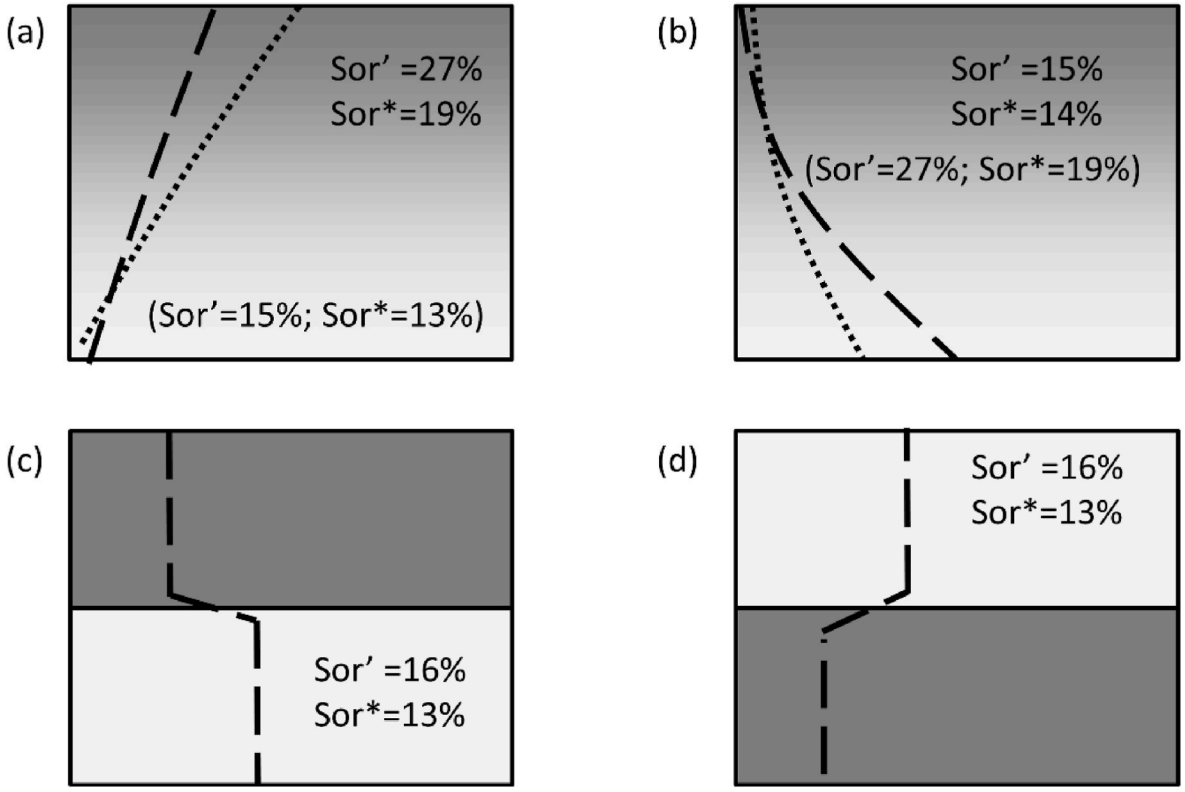

Fig. 14. Average Sor' (Eq. (44)) and estimated Sor value Sor* (Eq. (43)) for the six variable S_{or} models described in the main text. The grey scale is from 11% Sor (light grey) to 33% Sor (dark grey). The dashed lines are the approximate positions of the peak of the ethyl acetate concentration at 9.3 [d], i.e., when back production starts while the dotted line in (a) and (b) refers to models 5 and 6, respectively. (a): model 1; the values in parentheses refer to model 5. (b): model 2; the values in parentheses refer to model 6; (c): model 3; (d): model 4.

parameters that are ignored in the present study.

Fig. 14 depicts the results for variable S_{or} scenarios. The S_{or}* estimates are 1–3% lower than S_{or}'. S_{or}' may tend to underestimate the true average S_{or}, so the error is perhaps slightly larger. However, for models 1 and 3, S_{or}* is 8% too low. These are the two models where S_{or} increases with increasing porosity. More work is required to understand this phenomenon. Since any real oil-bearing formation will have spatially variable porosity, permeability and S_{or}, this result suggests that care must be executed in cases where these variations are large.

The results for the four 'standard' (constant S_{or}) models (Fig. 10) but with pre-flushing to 6 m from the wellbore are illustrated in Fig. 15. There is no discernible difference between the peaks in the tracer concentrations (Eq. (43)), except, of course, that production starts at different times ((a) and (b) are equal in this sense since the average porosity are the same.) In all cases, S_{or} is 4% too low – i.e., within the typical error range for the models with no pre-injection. Thus, with the assumptions used, pre-flushing has no significant effect on S_{or}*in our models. .

3. Conclusions

Pedersen (2021) presented the first SWCT model that included temperature gradients across the primary tracer bank, pH driven hydrolysis changes when pH buffering by solutes in the injected brine or calcite in the rock matrix are accounted for, as well as diffusion and dispersion. Here, we have developed this model further by considering large porosity, permeability and S_{or} variations in the target formation. The new models include turbulent flow in the wellbore coupled to fluid flow in the porous oil-bearing formation. Both coarsening and fining upwards sequences as well as constant porosity scenarios were investigated. We considered only sandstones with calcite cement and a brine composition realistic for such a reservoir.

Our principal conclusion is that coarsening and fining upwards porosity and permeability distributions have no significant impact on the S_{or}* estimates relative to models with constant values – Eq. (43) systematically underestimates S_{or} by 2–4% as it does for constant porosity and permeability scenarios. This is also the case with spatially variable S_{or}, except in two models where S_{or} increases with increasing porosity and permeability – then we find a significantly larger error of 8%. More work is needed to understand this effect. One way forward could be to combine pore scale numerical models of a SWCT test with tracer laboratory tests using either packed columns or cores with variable S_{or}.

pH buffering is efficient in our sandstone with calcite cement scenarios, and pH is lowered by only 0.3 units or less. Consequently, it is temperature that governs the rate of hydrolysis of the primary tracer.

The bulk of ethanol is generated during shut-in contrary to the conclusions in Wellington and Richardson (1994a, 1994b, 1994c), but in agreement with the conclusions of Ghosh (1994), Deans and Ghosh (1994) and Pedersen (2020, 2021).

Pre-flushing has no appreciable effect on S_{or}* in the four scenarios investigated in this study. Although these calculations do not consider multicomponent or two-phase effects, we expect that the result would have been quite similar if these factors had been included. Further work is needed to evaluate this hypothesis.

Credit author statement

Tom Pedersen developed the concept presented in the paper, established the methodology, did all the programming, wrote the original paper and performed the revision.

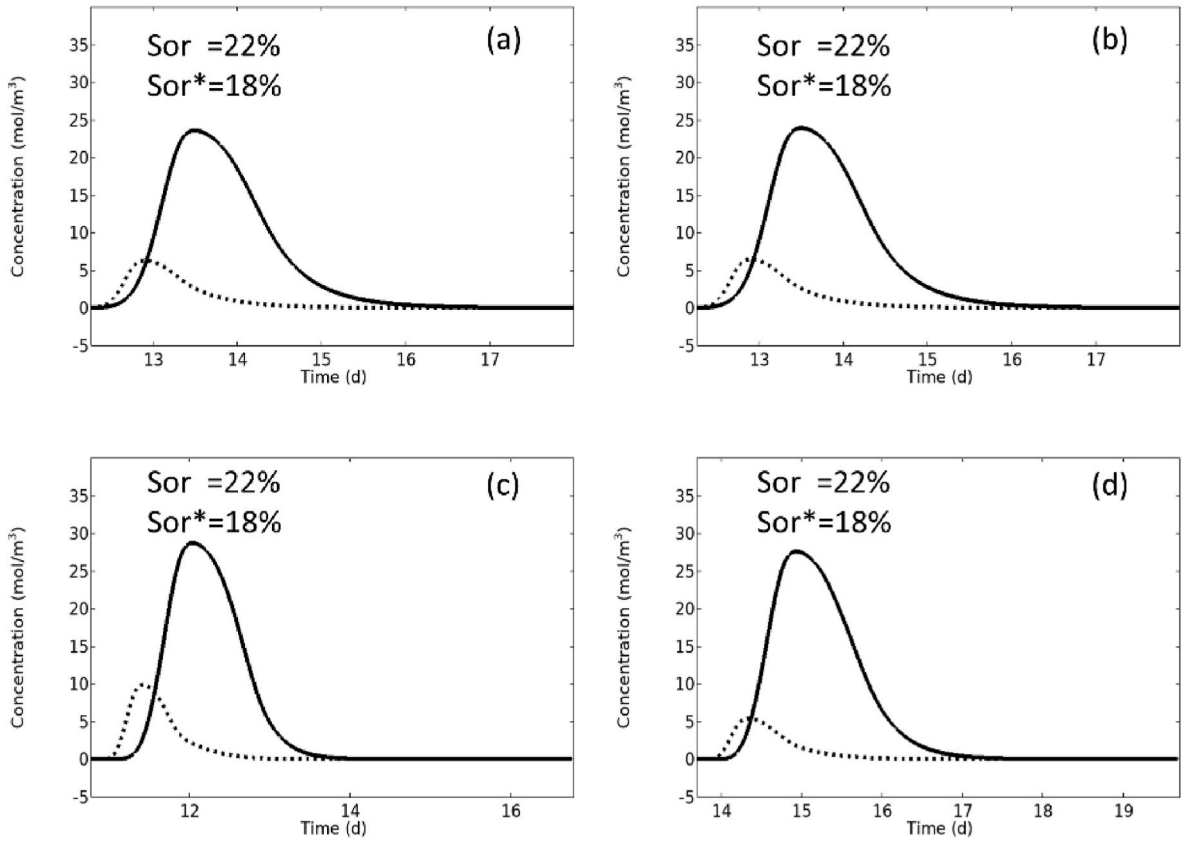

Fig. 15. Synthetic tracer production curves as functions of time starting at the end of shut-in. The solid curve is for ethyl acetate and the dashed is for ethanol. Also included is the S_{or}* value from Eq. (43). (a): coarsening upwards. (b) fining upwards. (c): constant porosity (10%) and permeability (1 mD). (d): constant porosity (30%) and permeability (1000 mD).

Declaration of competing interest

The authors declare that they have no known competing financial interests or personal relationships that could have appeared to influence the work reported in this paper.

Acknowledgements

The author has no real or perceived conflicts of interest. The data used can be found in publications referenced in the paper. Institute for Energy Technology supported this work financially.

References

Al-Shalabi, E.W., Luo, H., Delshad, M., Sepehrnoori, K., 2017. Single-well chemical tracer modeling of low salinity water injection in carbonates. SPE Reservoir Eval. Eng. 20 (1), 118–133. https://doi.org/10.2118/110228-PA. SPE-173994-PA.

Bandura, A.V., Lvov, S.N., 2006. The ionization constant of water over wide ranges of temperature and density. J. Phys. Chem. Ref. Data 35 (1), 15–30.

Bars, M.L., Worster, M.G., 2006. Interfacial conditions between a pure fluid and a porous medium: implications for binary alloy solidification. J. Fluid Mech. 550, 149–173.

Bear, J., 1979. Hydraulics of Groundwater. McGraw-Hill.

Carlisle, C., Al-Maraghi, E., Al-Saad, B., Britton, C., Fortenberry, R., Pope, G., 2014. One-spot pilot results in the Sabriyah-Mauddud carbonate formation in Kuwait using a novel surfactant emulsion. In: Presented at the SPE Improved Oil Recovery Symposium. https://doi.org/10.2118/169153-MS. Tulsa, Oklahoma, USA, April 2014. SPE-169153-MS.

Chang, M.M., Maerefat, N.L., Tomutsa, L., Honarpour, M.M., 1988. Evaluation and comparison of residual oil determination techniques. SPE Evaluation 3 (1), 251–262. https://doi.org/10.2118/14887-PA. SPE-14887-PA.

Coats, K.H., Smith, B.D., 1964. Dead-end pore volume and dispersion in porous media. SPE J. 647, 73–84.

Cockin, A.P., Malcolm, L.T., McGuire, P.L., Giordano, R.M., Sitz, C.D., 2000. Analysis of a single-well chemical tracer test to measure the residual oil saturation to a hydrocarbon miscible gas flood at prudhoe bay. SPE Reservoir Eval. Eng. 3 (6), 544–551. https://doi.org/10.2118/68051-PA. SPE-68051-PA.

COMSOL Multiphysics, 2020. User Guide.

Cook Jr., C.E., 1971. Method of determining fluid saturations in reservoirs. US Patent No 3, 590–923.

Deans, H.A., 1971. Method of determining fluid saturations in reservoirs. U.S. Patent No. 3, 623–842.

Deans, H.A., Majoros, S., 1980. The Single-Well Chemical Tracer Method for Measuring Residual Oil Saturation. Final report, Contract No. DE-AS19-79BC20006. US DOE, Houston, Texas. October 1980.

Deans, H.A., Carlisle, C.T., 1986. Single-well tracer tests in complex pore systems. In: Presented at the SPE Enhanced Oil Recovery Symposium. https://doi.org/10.2118/14886-MS. April 20–23, 1986. SPE-14886-MS.

Deans, H.A., Ghosh, R., 1994. pH and reaction rate changes during single-well chemical tracer tests. In: Presented at the SPE/DOE Improved Oil Recovery Symposium. https://doi.org/10.2118/27801-MS. April 17–20, 1994. SPE-27801-MS.

Deans, H.A., Carlisle, C., 2007. The single-well chemical tracer test – a method for measuring reservoir fluid saturations in situ. In: Holstein, E.D. (Ed.), Petroleum Engineering Handbook, Reservoir Engineering and Petrophysics, vol. V. Society of Petroleum Engineers, Richardson, Texas, pp. 615–649.

Doorwar, S., Tagavifar, M., Dwarakanath, V., 2020. A 1D Analytical Solution to Determine Residual Oil Saturations from Single-Well Chemical Tracer Test. https://doi.org/10.2118/200420-MS. This paper was prepared for presentation at the SPE Improved Oil Recovery Conference originally scheduled to be held in Tulsa, OK, USA, 18 – 22 April 2020. Due to COVID-19 the physical event was postponed until 31 August – 4 September 2020 and was changed to a virtual event. SPE-200420-MS.

Fortenberry, R., Suniga, O., Delshad, M., Singh, B., Alkaaoud, H.A., Carlisle, C.T., Pope, G.A., 2016. Design and demonstration of new Single-Well Tracer Test for viscous chemical Enhanced-Oil-Recovery fluids. SPE J. 21 (4), 1075–1085. https://doi.org/10.2118/178914-PA. SPE 178914-PA.

Gadgil, A., 1979. The Single-Well Chemical Tracer Test in Petroleum Reservoirs with Multicomponent, Two-phase Flow Effects. Master thesis. Rice University, Houston, Texas (August 1979).

Ghosh, R.S., 1994. Effects of pH on Tracer Reaction (Ester Hydrolysis) Rate in Single Well Chemical Tracer Test for Residual Oil Saturation – a Quantitative Approach. Master thesis, University of Wyoming, Laramie, Wyoming (May 1994).

Hiatt, E.E., 2000. Sedimentology and sequence stratigraphy in basin analysis and paleohydrologic studies. In: Kyser, K. (Ed.), Fluids and Basin Evolution. Mineralogical Association of Canada, Ottawa, Canada, pp. 19–38.

International Critical Tables, 1930, first ed. Natl. Research Council, McGraw-Hill Book Co. Inc., New York City, VII.

Kazemi, N., Korrani, A., Jerauld, G., Al-Qattan, A., 2019. Improved interpretation of single-well-chemical-tracer for low salinity and polymer flooding. In: Paper Presented at the SPE Kuwait Oil & Gas Show and Conference. https://doi.org/10.2118/198022-MS. October 13–16, 2019. SPE-198022-MS.

Khaledialidusti, R., Kleppe, J., 2018. Significance of geochemistry in single-well chemical-tracer tests by coupling a multiphase-flow simulator to the geochemical package. SPE J. 23 (4), 1126–1144. https://doi.org/10.2118/189971-PA. SPE-189971-PA.

Khaledialidusti, R., Kleppe, J., Enayatpour, S., 2014. Evaluation and comparison of available tracer methods for determining residual oil saturation and developing an innovative single well tracer technique: dual salinity tracer. In: Paper Presented at the International Petroleum Technology Conference. https://doi.org/10.2523/IPTC-17990-MS. December 10–12, 2014. IPTC-17990-MS.

Khaledialidusti, R., Kleppe, J., Skrettingland, K., 2015. Numerical interpretation of single well chemical tracer (SWCT) tests to determine residual oil saturation in Snorre Reservoir. In: Presented at the EUROPEC 2015. https://doi.org/10.2118/174378-MS. June 1–4, 2015. SPE- 174378-MS.

Millington, R.J., Quirk, J.M., 1961. Permeability of porous solids. Trans. Faraday Soc. 57, 1200–1207.

Park, Y.J., 1989. Thermal Effects of Single-Well Chemical Tracer Tests for Measuring Residual Oil Saturation. PhD dissertation. University of Houston, Houston. May 1989.

Park, Y.J., Deans, H.A., Tezduyar, T.E., 1991. Thermal effects on single-well chemical tracer tests for measuring residual oil saturation. SPE Form. Eval. 6 (3), 401–408. https://doi.org/10.2118/19683-PA. SPE-19683-PA.

Pedersen, T., 2018. Properly designed temperature history nanoparticles may improve residual oil saturation estimates from SWCT tests. J. Petrol. Sci. Eng. 170, 383–391.

Pedersen, T., 2020. Temperature gradient and pH effects on Sor estimates from SWCT tests - the no buffer case. J. Petrol. Sci. Eng. 196 https://doi.org/10.1016/j.petrol.2020.107652.

Pedersen, T., 2021. A Single Well Chemical Tracer model that accounts for temperature gradients, pH changes and buffering. J. Petrol. Sci. Eng. 201 https://doi.org/10.1016/j.petrol.2021.108500.

Plummer, L.N., Busenberg, E., 1982. The solubilities of calcite, ankerite and vaterite in CO_2-H_2O solutions between 0 and 90 °C, and an evaluation of the aqueous model for the system $CaCO_3$-CO_2-H_2O. Geochem. Cosmochim. Acta 46, 1011–1040.

Ramey Jr., H.J., 1962. Wellbore heat transmission. J. Petrol. Technol. 96, 427–435. https://doi.org/10.2118/96-PA. SPE-96-PA.

Ramon, J.C., Cross, T., 1997. Characterization and prediction of reservoir architecture and petrophysical properties in fluvial channel sandstones, Middle Magdalena Basin, Colombia. C.T. F Ciencia, Tecnol., Futuro 1 (3), 19–46.

Shook, G.M., Pope, G.A., Asakawa, K., 2009. Determining reservoir properties and flood performance from tracer test analysis. In: Paper Presented at the SPE Annual Technical Conference and Exhibition. https://doi.org/10.2118/124614-MS. October 4–7, 2009. SPE-124614-MS.

Skrettingland, K., Holt, T., Tweheyo, M.T., Skjevrak, I., 2010. Snorre low salinity water injection – core flooding and Single Well field pilot. SPE Reservoir Eval. Eng. 14 (2), 182–192. https://doi.org/10.2118/129877-PA. SPE-129877-PA.

Tomich, J.F., Dalton Jr., R.L., Deans, H.A., Shallenberger, L.K., 1973. Single-well tracer method to measure residual oil saturation. J. Petrol. Technol. 25 (2), 211–218. https://doi.org/10.2118/3792-PA. SPE-3792-PA.

Wellington, S.L., Richardson, E.A., 1994a. Redesigned ester single-well tracer test that incorporates pH-driven hydrolysis rate changes. SPE Reservoir Eng. 9 (4), 233–239. https://doi.org/10.2118/24135-PA. SPE-24135-PA.

Wellington, S.L., Richardson, E.A., 1994b. A single-well tracer test with in-situ-generated CO_2 as the oil tracer. SPE Reservoir Eng. 9 (2), 85–91. https://doi.org/10.2118/22904-PA. SPE-22904-PA.

Wellington, S.L., Richardson, E.A., 1994c. Simultaneous use of ester and CO_2 single-well tracers. SPE Reservoir Eng. 9 (4), 240–246. https://doi.org/10.2118/29226-PA. SPE-29226-PA.